Influence of Process Parameters on Properties of Super Invar Alloy Fabricated by Laser Powder Bed Fusion for Semiconductor Equipment

Renjie Zhao[a,b], Yakai Zhao[c], Meng Qin[a], Yubo Jia[a], Kai Feng[a*], Zhuguo Li[a*], Upadrasta Ramamurty[c,d], Renbiao Xie[b]

a Shanghai Key Laboratory of Materials Laser Processing and Modification, School of Materials Science and Engineering, Shanghai Jiao Tong University, Shanghai, 200240, China

b Shanghai Micro Electronics Equipment (Group) Co., Ltd, Shanghai, 200120, China

c Institute of Materials Research and Engineering (IMRE), Agency for Science, Technology and Research (A*STAR), Singapore, 138634, Republic of Singapore

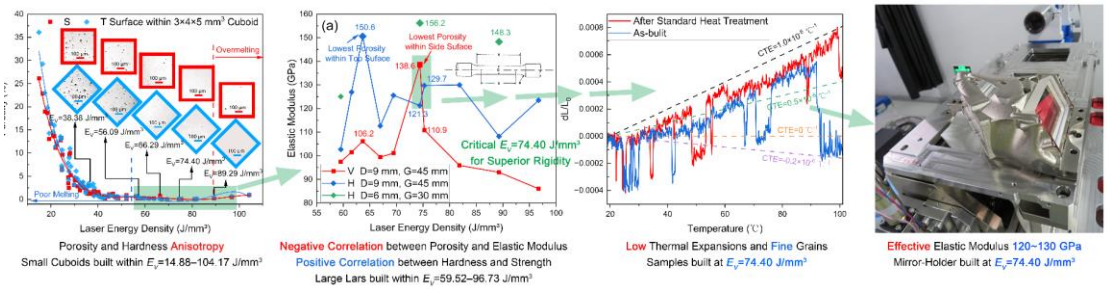
d School of Mechanical and Aerospace Engineering, Nanyang Technological University, Singapore, 639798, Republic of Singapore

*Corresponding Author:

E-mail address: fengkai@sjtu.edu.cn (Kai Feng)

E-mail address: lizg@sjtu.edu.cn (Zhuguo Li)

Graphical abstract:



Abstract: Super Invar alloy has drawn much attention for utilization in semiconductor equipment and other high-precision devices due to its even lower coefficient of thermal expansion than classical Invar 36. In this paper, a detailed study for the influence of process parameters combined with building sizes on the microstructures, porosities, hardnesses, tensile and thermal behaviors of multi-size Super Invar samples fabricated by laser powder bed fusion (LPBF) is conducted. The poor thermal conductivity of Super Invar leads to distinctive critical laser energies for full melting between spacings and layers. A positive correlation between the tensile strength and the hardness, and a negative correlation between the elastic modulus and the porosity within the areas parallel to tensile direction are identified. The increase of building size or volume apparently leads to more porosity, higher hardness, higher tensile strength, lower elongation, and lower horizontal elastic modulus of LPBF processed Super Invar alloy. The as-fabricated and standard-heat-treated Super Invar samples show very low coefficients of thermal expansion within 20–100 °C. The selected optimum parameter for comprehensive properties concerned in semiconductor equipment was employed to build a Super Invar mirror-holder used in the lithography machine, and its part stiffness performance was validated with an effective elastic modulus of 120–130 GPa.

Keywords: Super Invar, Laser Powder Bed Fusion (LPBF), Parameter Selection, Modal Analysis, Elastic Modulus, Semiconductor Equipment

1 Introduction

The coefficient of thermal expansion (CTE) of the Super Invar (Fe-32Ni-4Co) alloy, developed by Masumoto in 1929, is even lower of than that of the Invar 36 (Fe-36Ni) alloy[1-4], which is the most studied and commercially used. As a result, it has been applied for fabricating core structural components of semiconductor manufacturing equipment to satisfy the strict requirements associated with the high-precision manufacturing[5]. Considering the ambient-temperature, non-heavy-load, and long-term working conditions of these multi-dimensionally ultra-high-precision components in photolithography equipment and many other precision mechanical systems[6], attention is paid to their dimensional stability under stress, time, and temperature variations, rather than their engineering strength[7]. It should be noted that, for identical shapes, the part stiffness, indicating its ability to guarantee accurate positioning and minimal deflection under external loads or forces, is proportional to the elastic modulus (E) and negatively correlated with material density (ρ)[8, 9]. Therefore, the E, temporal stability, and CTE near room temperature are fundamental material properties for engineering estimation in semiconductor equipment, despite the complex macro-geometry of these high-stiffness components. Nevertheless, the E of wrought Super Invar (~144 GPa) is dramatically lower than that of stainless steel (~200 GPa) despite similar densities of these two materials[2, 10, 11]. This drawback greatly limits the high-stiffness structural applications of the Invar alloy despite its low CTE in semiconductor equipment.

Typically, these core structural components are designed into complex shapes such that they have high stiffness, to compensate for the poor E of the Super Invar alloy. However, machining from bulks into complex parts is not only time consuming, but also very expensive[12], especially since Super Invar has high ductility, high work hardening, and poor heat conductivity, making it difficult to machine[13, 14].

Laser powder bed fusion (LPBF), a recent near-net-shape metal additive

technology, is expected to increase the material utilization ratio, reduce the machining difficulty, accelerate delivery time, and save product costs[15-20]. Besides, the powerful free-form capability of this layer-by-layer building process also enables engineers to free themselves from the limits of traditional processes, and thus realize more complicated high-stiffness design with even greater freedom[21-25].

Almost all the previous studies have focused on the classical Invar 36 fabricated by LPBF. Qiu *et al*. first examined a wide LPBF parameter window for obtaining a low porosity (<0.5%) Invar 36 alloy[26], and then added TiAl particles into it for developing intermetallic nano-particles reinforced alloy[27]. Yakout *et al*.[28-31] studied the LPBF parameter selection of Invar 36 alloy via tensile tests (as-built size: Φ94 mm×16 mm), density and thermal expansion measurements, and claimed the optimum energy density is 86.8 J/mm^3. Harrison *et al*. [32], Asgari *et al*.[33], and Yang *et al*.[34] investigated the influence of LPBF parameters on thermal expansion properties of Invar 36. Wei *et al*.[35] studied the mechanical properties of the Invar 36 samples (as-built size: Φ25 mm×20 mm) at room temperature, 200 and 600 ℃, and recommended the optimal laser energy density to be 99.2 J/mm^3. Wegener *et al*.[36] investigated the microstructure and ambient-temperature mechanical behavior of the LPBF Invar 36 specimens (as-built size: 20×10×31 mm^3) under monotonic and cyclic loading. Hitzler *et al*.[37] studied the temperature-dependent elastic modulus of the LPBF Invar 36 bars (as-built size: Φ10 mm×70 mm). Yang *et al*.[38] explored the influence of microstructures and porosity on the mechanical properties of the LPBF Invar 36 sheets (as-built size: 135×13×3.5 mm^3) using the *in-situ* X-ray computed tomography. Huang *et al*.[39] revealed the anisotropy of microstructure, mechanical properties and thermal expansion of the LPBF Invar 36 alloy (Tensile specimen size: Φ12 mm×62 mm).

In most of the aforementioned studies, the selection criteria for optimum LPBF process parameters are based mainly on the density, tensile strength, and CTE in combination with microstructure without any consideration of the *E*, which is the main concern in semiconductor equipment and many other high-precision devices. It should

also be noted that only small-size (commonly less than 100 mm) Invar alloy specimens were prepared by very limited parameter combinations within a relatively wide studied range for LPBF parameter selection, especially considering the critical effect of heat accumulation during LPBF on as-built material properties extensively investigated for a variety of alloys[40-43]. The influence of the building volume or geometry on properties of LPBF processed Invar alloy also have been largely overlooked despite the fact that the Fe-Ni Invar alloy family shows extremely poor heat conductivity, given that LPBF is a high-temperature laser-processing technique[44]. Therefore, the identified optimum parameters remain to be verified on complex-shaped and different-size components.

Keeping the above in view, the mechanical properties, especially the hardness and elastic modulus, combined with microstructure and thermal expansion behaviors of multi-size specimens processed by different sets of LPBF parameters were characterized in detail to identify the intrinsic connection between LPBF parameters, build sizes, and material properties of as-built Super Invar alloy. The selected optimum parameters for application consideration of low-thermal-expansion and high-stiffness performance in semiconductor equipment were utilized to build a mirror-holder used in our lithography machines. Part performance of this component is experimentally evaluated and discussed based on unique material properties of LPBF processed Super Invar alloy.

2 Experimental

2.1 SLM process

The Super Invar alloy samples examined in this study were all additively built using an EOS M 290 LPBF machine equipped with a 400W ytterbium fiber laser in argon atmosphere to minimize oxidation during processing. The pre-alloyed Super Invar powders were prepared by the Shanghai Electric Group Co., Ltd. Central Academe (Shanghai, China) via gas atomization. For LPBF, while laser power (P) and

scanning speed (v) were altered from sample to sample, as illustrated in Figure 1, the following parameters were kept constant: 0.04 mm layer thickness (t), 0.12 mm hatch spacing, 10 mm stripe width, and the stripe scanning strategy with 0.08 mm stripe overlap and 67° scan rotation between successive layers. Stainless steel 316L substrates were used and pre-heated to 100 °C in each Super Invar LPBF job. 72 combinations of P and v were selected to realize a wide range of laser energy densities, E_V ($=P/(v\times h\times t)$), of 14.88–104.17 J/mm^3. In total, 72 3×4×5 mm^3 cuboids, 10 16×16×150 mm^3 bars, 10 150×16×16 mm^3 bars, and 3 100×10×10 mm^3 bars were fabricated using the parameters listed in **Fig. 1**. The optimum parameters, especially for superior rigidity performance of LPBF processed Super Invar alloy, were identified through these prints. Thereafter, these optimum parameters, which will be discussed later in this paper, were used to build two 60×10×10 mm^3 blocks for further investigation on the thermal expansion properties and a mirror-holder, one of the core components used in the lithography machines for final application verification.

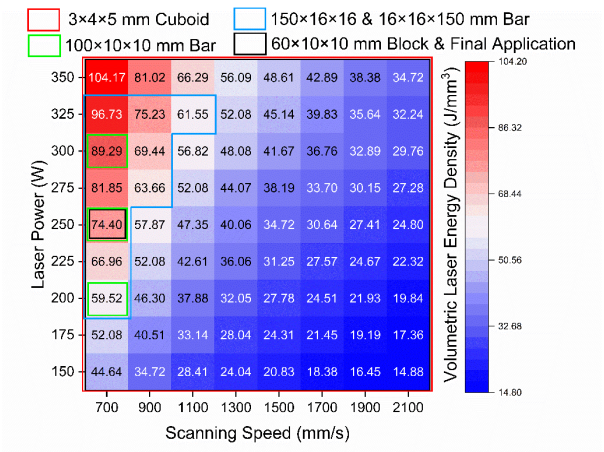


Fig. 1. Volumetric laser energy densities with different LPBF process parameters.

The as-built and machined samples with different-specifications are illustrated in **Fig. 2**(a). Samples with same dimensions were built in one LPBF job to eliminate the potential variations associated within different printing jobs. As **Fig. 2**(b) displays, the vertical-built (16×16×150 mm^3) and horizontal-built (150×16×16 mm^3) elongated bars are all fabricated together on one substrate, for instance.

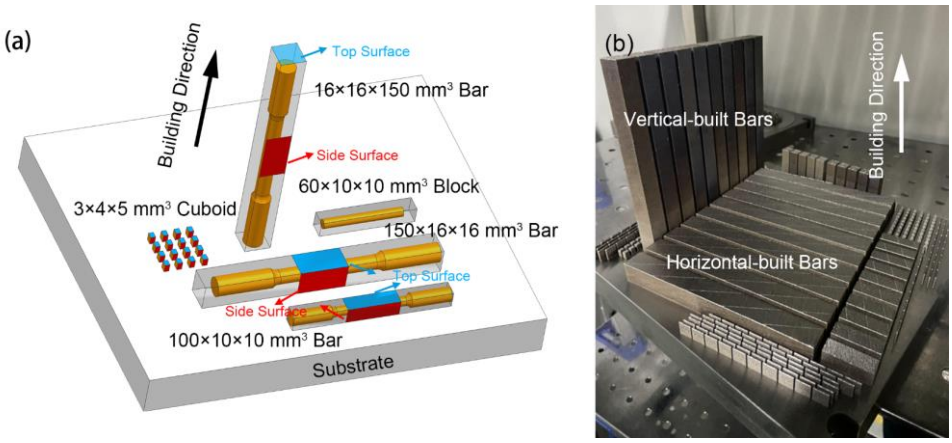


Fig. 2. (a) Schematic diagram of LPBF samples, (b) as-built Super Invar bars in one LPBF job

2.2 Porosity measurement and indentation tests

In addition to the cuboids, both the side and top surfaces (marked with red and blue, respectively, in **Fig. 2**(a)) of the elongated bars were also ground and polished to conduct metallographic examination and hardness tests before tensile test specimen machining. The observed middle areas on the bar samples are illustrated in **Fig. 2**(a). The porosities of both surfaces were then quantified using the image analysis performed with the commercial Image-Pro software. Following the ASTM E384 standard[45], Vickers hardness was measured using a Shanghai Taiming HXD-2000TMJC/LCD micro-Vickers hardness tester with a load of 9.80 N and a hold time for 10 s. At least 5 tests were conducted per condition.

2.3 Tensile tests and fracture analysis

After porosity observation and hardness tests, these as-built Super Invar bars were machined to dog-bone shaped samples for tensile tests (45 mm gauge length and 9 mm gauge diameter from the 16×16×150 mm^3 and 150×16×16 mm^3 bars; 30 mm gauge length and 6 mm gauge diameter from the 100×10×10 mm^3 bars) according to the ASTM standards: F3122-14[46] and E8/E8M-16a[47]. The gauge lengths are equal to five

times the nominal diameter. All the tensile tests were performed at room temperature using a Zwick/Z100 tensile-testing machine under a nominal strain rate of 5×10^{-4} s^{-1}. The stress-strain curves were recorded for obtaining the tensile yield strength (YS), the ultimate strength (UTS), *E*, and the elongation to failure. Tensile fractured surfaces and the longitudinal sections of tested specimens were examined using scanning electron microscopy (SEM), energy dispersive X-ray spectroscopy (EDX), and electron backscatter diffraction (EBSD) in an FEI NOVA Nano SEM 230 SEM.

2.4 Microstructural characterization

The Super Invar powder characteristics was revealed using a JSM-6510 Series scanning electron microscope. The powder size distribution was determined by the laser diffraction method using a Mastersizer 3000 particle size analyzer. The composition of the as-received powder was quantitively analyzed using a CISRI NSC Plasma 2000 Inductively Coupled Plasma Optical Emission Spectrometer (ICP-OES), a CISRI NSC Plasma 2000 Carbon/Sulfur analyzer, and a CISRI NSC ONH5500 Oxygen/Nitrogen/Hydrogen analyzer.

The microstructures of side and top surfaces within fabricated cuboids and bars were prepared with a standard metallographic method and analyzed using a Zeiss Axio Imager A2m optical microscope (OM). Etching was performed with a solution containing 75% HCl and 25% HNO_3 and an etching time of 20 s.

The X-ray diffraction (XRD) technique was used in a Bruker D8 Advance da Vinci with Cu-Kα radiation to determine the phase compositions of both the Super Invar powder and as-built samples. To compare the microstructures of the samples built to different scales, the as-built cuboids, horizontal-built $150\times16\times16$ mm^3 and vertical-built $160\times15\times15$ mm^3 bars fabricated at low, medium and high laser energy densities (E_V = 59.52, 74.40,and 89.29 J/mm^3 respectively) were examined via XRD.

2.5 Thermal expansion measurement

The standard heat treatment process recommended per the Chinese YB/T 5241-2014 Standard for Super Invar has been adopted in this study, which includes heating from room temperature to 830 °C at the rate of 5 °C/min, dwell at 830 °C for 0.5 h prior to water quenching, and then heating to 315 °C at the rate of 5 °C/min, dwell at 315 °C for 1 h prior to air cooling, and finally soaking at 95 °C for 48 h[48]. Assuming that the Super Invar samples built with the same LPBF parameters present similar thermal expansion performances (despite the differences in their building geometries), we only investigated the CTEs of horizontal-built 60×10×10 mm^3 block samples in this study. Two cylindrical samples with a length of 50 mm and a diameter of 6 mm were machined from an as-built 60×10×10 mm^3 block and another standard heat-treated one as illustrated in **Fig. 2**(a). To study the influence of heat treatment on the CTE of the LPBF Super Invar alloy, thermal expansion measurements were performed on these two cylindrical samples between room temperature and 100 °C using a PerkinElmer TMA 4000 thermomechanical analyzer.

2.6 Impact hammer tests, modal simulation, and dimensional observations

The impact hammer test with an accelerometer is a fundamental modal analysis method for extracting dynamic information from measured frequency response function (FRF) data on small-sized components in the mechanical engineering field[49, 50]. To check the stiffness of the Super Invar mirror mount satisfies one of the critical application verification criteria, free-frequencies of this LPBF Super Invar component were experimentally identified according to the excitation frequency map[51]. They were also analyzed using the finite element analysis (FEA) method considering different sets of physical parameters in for comparison with the impact hammer test results.

Considering the long-term dimensional growth effect widely observed within the

Fe-Ni Invar family (Invar 36 sample elongates ~1.0 ppm/year while the Super Invar below 0.001 ppm/year at 27 °C)[52, 53], all these critical dimensional features of the fine-machined mirror-holder were measured once a year using a Zeiss PRISMO Coordinate Measuring Machining (CMM) over a period of three years to study the temporal dimension stability of the LPBF Super Invar components for rigorous engineering use.

3 Results and discussion

3.1 Powder characteristics

The characteristics results of as-received powder are shown in **Fig. 3**. **Fig. 3**(a) displays the morphology of Super Invar powders and suggests that the powder particles are near-spherical with smooth surfaces. The powder size ranges in approximately 14–45 μm without obvious overly large or small particles, as presented in **Fig. 3**(b).

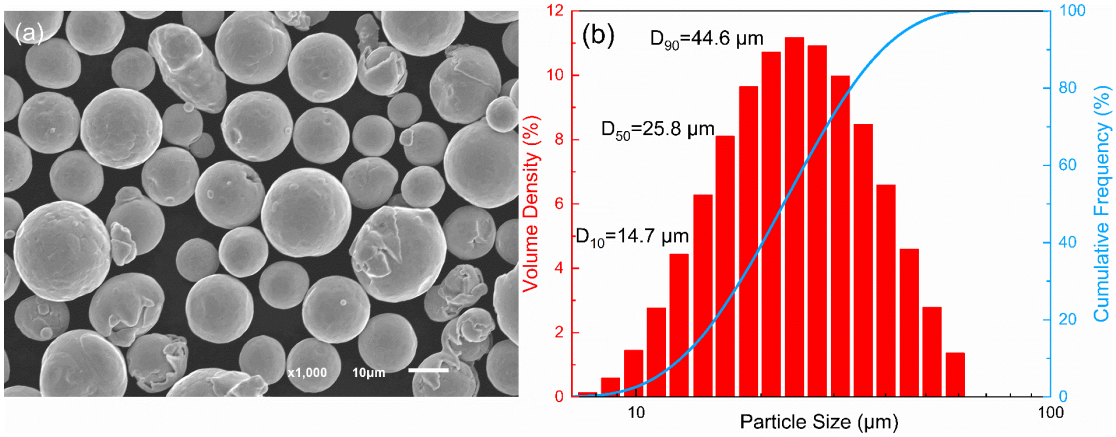


Fig. 3. (a) SEM image and (b) particle size distribution of the virgin Super Invar powder

3.2 Chemical analysis and crystallographic characterization

Extensive prior research has revealed that the CTE of the alloys in the Fe–Ni Invar system is highly sensitive to the composition[4, 54]. Therefore, besides chemical analysis conducted on the Super Invar powder using the ICP-OES spectrometer and element

analyzers, critical elements such Fe, Ni, and Co contents of as-built Super Invar cuboids and elongated bars at the highest laser energy densities in present study were also examined by using the EDX surface scanning for comparison. **Table 1** lists the results of the chemical composition analysis. Both the powder and as-fabricated samples' compositions conform to those specified by the 4J332 precision-alloy specification-designation according to Chinese GB/T 37797-2019 Standard[55]. Considering the significant EDX measurement error, especially for the Co content, the main constituent Fe, Ni, and Co elements could be judged unchanged within the studied laser energy range of 14.88–104.17 J/mm^3 during LPBF.

Table 1. Chemical composition of the Super Invar powder and as-built samples (in wt.%)

	Element	**Fe**	**Ni**	**Co**	**Cu**	**Mn**	**C**	**S**	**O**	**N**
Powder	wt.%	Bal.	32.5	3.78	0.56	0.50	0.021	0.0025	0.025	0.003
3×4×5 mm^3 Cuboid at E_V=104.17 J/mm^3	wt.%	63.8	31.1	5.1	-	-	-	-	-	-
16×16×150 mm Bar at E_V=96.73 J/mm^3	wt.%	63.9	31.6	4.5	-	-	-	-	-	-
150×16×16 mm Bar at E_V=96.73 J/mm^3	wt.%	63.9	32.0	4.1	-	-	-	-	-	-
4J332[55]	wt.%	Bal.	31.5–33.0	3.2—4.2	0.40—0.80	0.20—0.60	＜0.05	＜0.020	-	-

Yakout *et al.* [29] reported the vaporization and micro-segregation of Mn, Cr, and Ni within the LPBF Invar 36 fabricated with the laser energy densities higher than 86.8 J/mm^3. Liu *et al.*[56] revealed the strong heat accumulation of Invar 36 along the build direction. Considering the probable heat-induced chemical segregation caused by high E_V or large build geometry within Super Invar, the spatial compositional variations of the critical elements such as Fe, Ni, and Co contents of the as-built samples built at the

highest E_V with the corresponding maximum built geometry (3×4×5 mm^3 cuboid fabricated with E_V = 104.17 J/mm^3 in combination with 16×16×150 mm^3 and 150×16×16 mm^3 bars with E_V = 96.73 J/mm^3) were also examined using EDX. Results are shown in **Fig. 4**. It is obvious that the Fe, Ni, and Co are all uniformly distributed in these samples despite the differences in the build dimensions. Therefore, notwithstanding the poor heat conductivity of Super Invar alloy, LPBF is still a reliable process for manufacturing its components without any obvious chemical segregation.

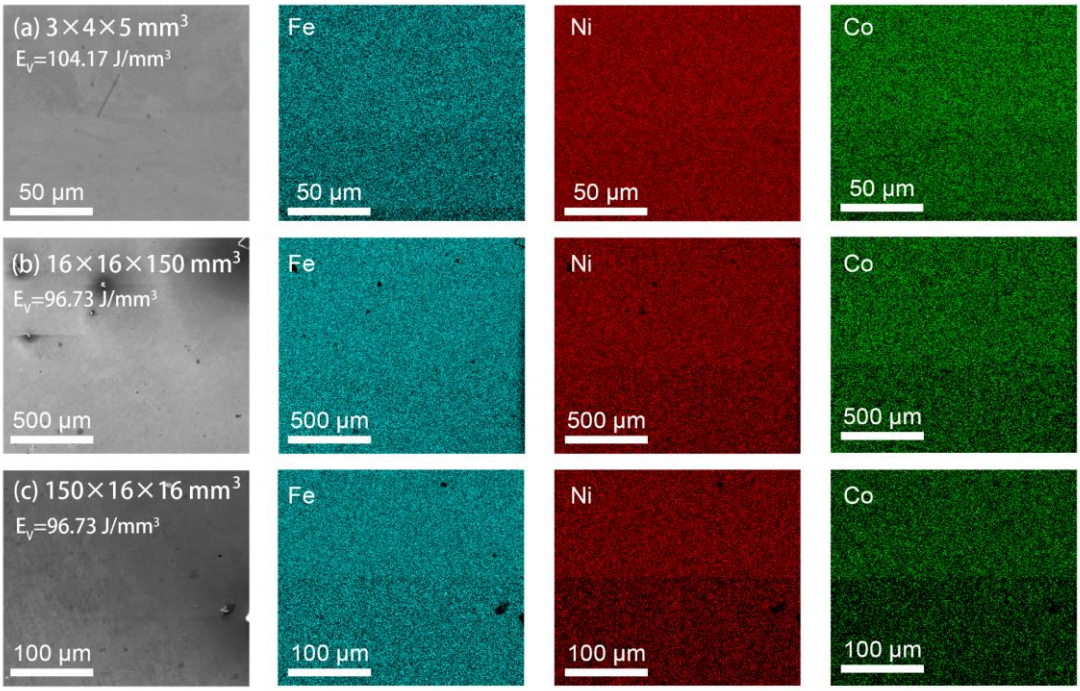


Fig. 4. EDX maps of the constituent Fe, Ni, and Co elements within (a) the cuboid, (b) 16×16×150 mm^3 vertical-built, and (c) 150×16×16 mm^3 horizontal-built elongated bars fabricated at the highest laser energy densities within this study.

Fig. 5 shows the XRD patterns of the Super Invar alloy powders and as-manufactured large-scale bar samples processed at relatively low, medium and high E_V. All the patterns show discernible reflections of Fe-Ni austenite γ-phase without the α-phase peaks. A similar phenomenon was also reported in LPBF processed Fe-36Ni alloy[26, 33, 35]. The reason may probably be that the volume fraction of α phase within the as-built Fe-32Ni-4Co samples is too low to be detected using the XRD technique

despite the addition of Co. Nevertheless, and quite different from the classical Invar 36's XRD patterns, faint reflections of the Co-Fe phase could be observed within the small cuboid fabricated at E_V = 59.52 J/mm^3 and clearly identified only within the horizonal-built 150×16×16 mm^3 bar fabricated at E_V = 74.40 J/mm^3. This observation indicates a strong dependence of the phase composition on the build shapes and LPBF parameters. It should be noted that these Co-Fe phase peaks could not be certainly found in the XRD patterns of cast or forged Super Invar alloy[3, 4, 57-59]. The possible mechanism for the abnormal dual-phase Super Invar alloys fabricated using LPBF at specific conditions is a subject for our future research.

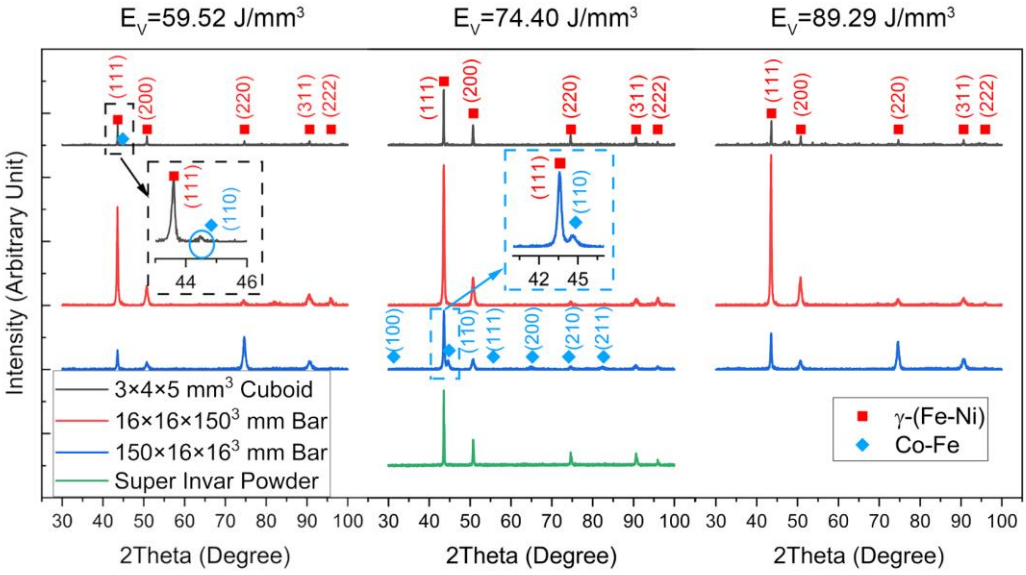


Fig. 5. X-ray diffraction patterns of the powder and as-built Super Invar samples at E_V = 59.52, 74.40, and 89.29 J/mm^3.

3.3 Porosity

Fig. 6 shows the porosity variations in side and top surfaces and typical metallographs of the as-built small cuboids (3×4×5 mm^3) and bars (16×16×150, 150×16×16, and 100×10×10 mm^3) as a function of E_V. Fig. **6**(a) clearly shows that porosity of the cuboid samples is strongly dependent on E_V, manifesting as lower

porosity with increasing E_V. The porosities measured on both the side and top surfaces are relatively high (>1.00 % in area fraction) when E_V < 38.38 J/mm^3. As E_V increases to 56.09 J/mm^3, the porosity of both surfaces decreases to 0.20 % and reaches a minimum value of 0.02–0.05% within E_V = 69.44–74.40 J/mm^3. However, pores start to be observable within the side surfaces of the cuboid samples when E_V exceeds 89.29 J/mm^3, indicating over-melting between layers along the build direction.

Besides, it is noticed that the porosity of the top surfaces is generally higher as compared to that on the side ones, at relative low level of E_V (＜52.08 J/mm^3). This anisotropy becomes muted with further increase in E_V, indicating a critical E_V for full melting between hatch spacings within top surfaces should be higher compared to that between build layers within side ones for small-scale parts.

Since the optimum range of E_V for obtaining dense Super Invar cuboids is between 66.29 to 89.29 J/mm^3, as deduced form the typical metallographic photographs displayed in Fig. **6**(a), this study selected 10 groups of parameter sets within the wider range of E_V in 59.52–96.73 J/mm^3 to identify the optimum E_V for mechanical properties as illustrated in **Fig. 1**.

Fig. 6(b) compares the porosity levels in the as-built cuboids and different-size bars. The bars were all found to show more defects than their small cuboid counterparts on both side and top surfaces. Similar phenomena were also observed in prior works[26, 27], where the scaling up of the Invar 36 and Ti-6Al-4V samples resulted in an increased porosity levels under certain processing conditions. Particularly, the porosity observed on the side surfaces is generally higher than those on the top ones in all the bar samples, especially when E_V decreases to below 74.40 J/mm^3, indicating the critical E_V for full layer melting. Fig. **6**(c) shows typical metallographs of observed areas within bars built in different directions with different sizes. More pores appear on the side surfaces, while fewer defects show up in the top surfaces in the vertical-built bars (16×16×150 mm^3) than in the horizontal-built ones (150×16×16 mm^3), revealing the positive correlation between observed surface porosity and its sectional dimension for a given build volume.

Besides, compared to the larger bars (16×16×150 and 150×16×16 mm^3), the small-scale horizontal-built ones show lower porosity levels on both the side and top surfaces, suggesting a negative correlation within porosity and built volume of the Super Invar alloy.

At E_V of 74.40 J/mm^3, the porosity levels on the side surfaces of cuboids and bars are still the lowest, despite different build heights or areas, whereas the optimum E_V for the top surfaces minimum porosity reduces from 74.40 to 69.44 J/mm^3, and then to 63.66 J/mm^3 for 3×4, 16×16, and 150×16 mm^2 cross-sectional build area samples, respectively. In conclusion, the optimum E_V for side surface is independent of the built area and is ~74.40 J/mm^3.

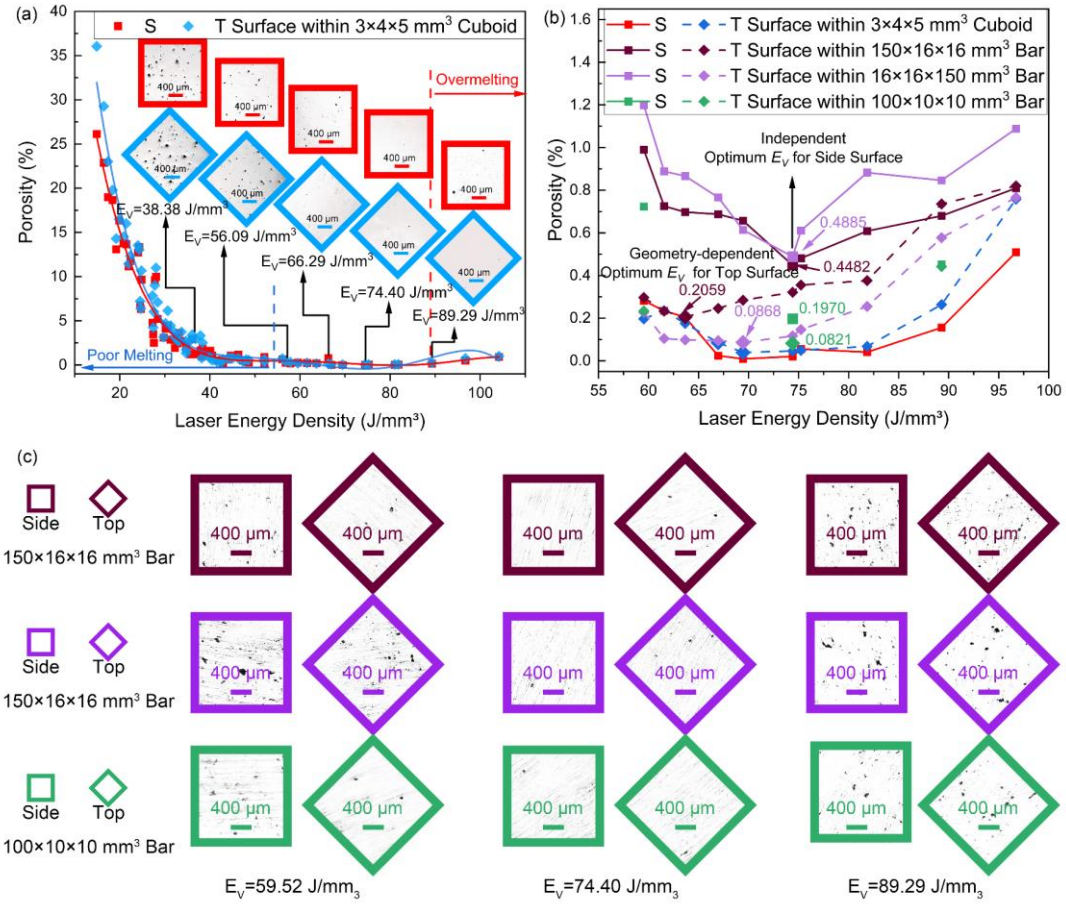


Fig. 6. Porosity variation with volumetric laser energy densities within side (S) and top (T) surfaces of (a) as-built cuboids (b) elongated bars and their counterpart cuboids, (c) metallographs of small-scale bars and their counterpart large-scale bars

3.4 Microstructural development

The microstructures of LPBF processed samples fabricated with different E_V were investigated with the aid of OM and SEM. The results are shown in **Fig. 7**. Comparing **Fig. 7**(a) and **Fig. 7**(c), the porosity anisotropy could be intuitively viewed at a relatively low E_V of 38.88 J/mm^3. The defects on the side surface could be identified as a small range of cracks and pores, while top surface shows thickly-dotted pores with different sizes due to poor melting within hatch spacings, as shown in **Fig. 7**(b) and (d). When E_V is increased to 61.55 J/mm^3, defects on the side and top surfaces, especially the latter, apparently decrease (compare **Fig. 7**(a) and (e) with **Fig. 7**(c) and (g)). The distributions of vertical columnar grains at E_V = 38.88–61.55 J/mm^3 are generally similar as shown in **Fig. 7**(b) and (f), while clusters of fine equiaxed grains could be observed only in the cuboid samples fabricated at a higher E_V, as shown in **Fig. 7**(d) and (h). All these features suggest that the critical E_V required for the complete melting in top surfaces should be higher than that on the side ones.

Porosity levels on the side surfaces are higher than those in top ones for large bars and cuboids fabricated at relatively high E_V values. This could be explained by comparing **Fig. 7**(i) with (j) and **Fig. 7**(f) with (h). The horizontal section of the acicular or elliptical cracks along or oblique to the vertical direction is near-spherical when viewed from the top. It should also be emphasized that the fraction of cracks decreases as the build height increases, as presented in **Fig. 7**(a) and (c), indicating the strong heat accumulation along the build direction at the height of only 5 mm. This observation agrees well with the simulation and experimental results that the surface temperature rises rapidly with the increasing build height, especially within the first tens of layers. (A total of 125 layers were present for the build height of 5 mm with layer thickness of 0.04 mm, in present study)[43, 60]. The poor thermal conductivity of Super Invar alloy and the localized nature of energy input from the laser heat source during LPBF causes the variation of the thermal histories from location to location, leading to very different

region-dependent material properties especially for Super Invar parts with large LPBF build volumes.

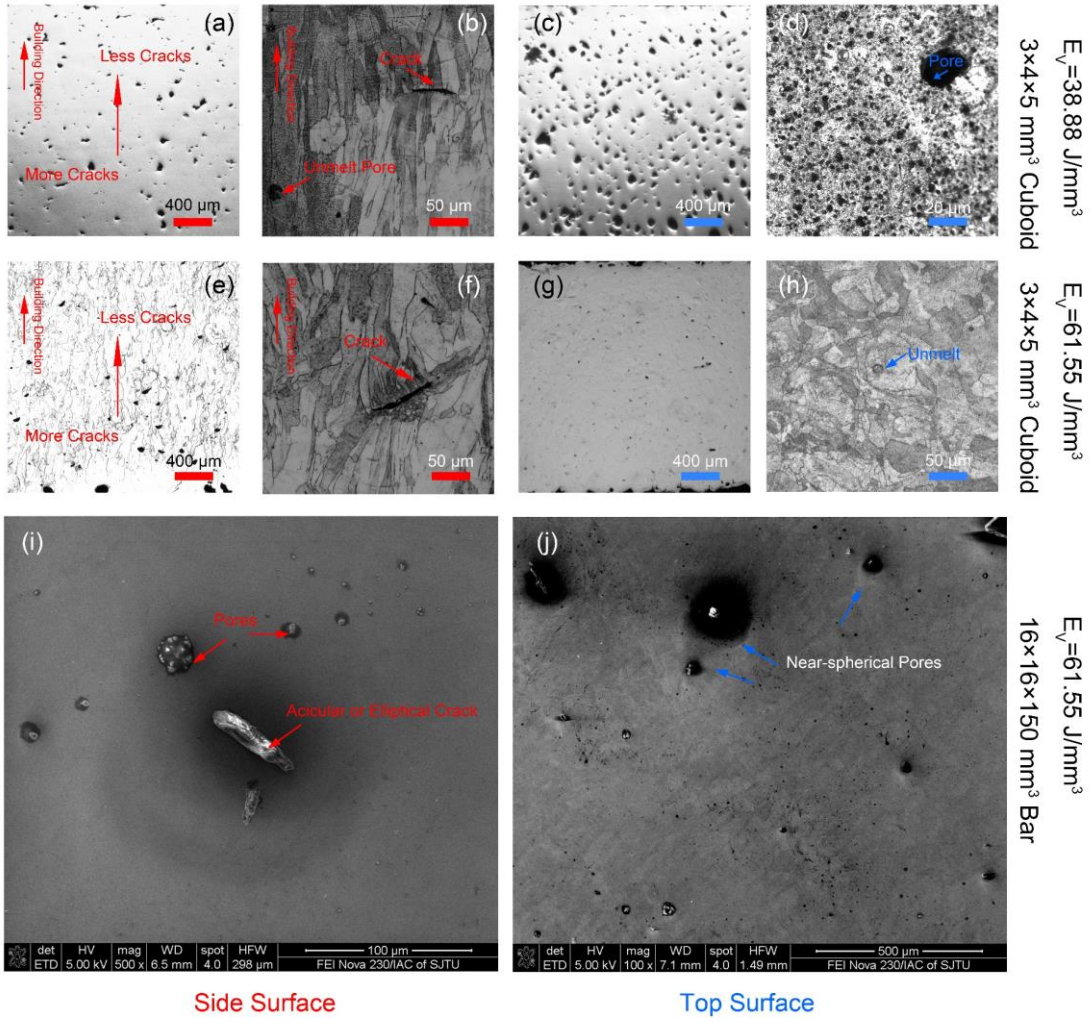


Fig. 7. metallographs of (a) (b) side surface and (c) (d) top surface of the cubic sample fabricated at E_V = 38.88 J/mm^3, metallographs of (e) (f) side surface and (g) (h) top surface in cubic sample fabricated at E_V = 61.55 J/mm^3, SEM photos of (i) side surface and (j) top surface of the large bar sample fabricated at E_V = 61.55 J/mm^3.

3.5 Hardness

Fig. 8 shows the variation of Vickers hardness in the top and side surfaces of as-built small cuboid samples (3×4×5 mm^3) and bars (16×16×150, 150×16×16, and 100×10×10 mm^3) as a function of E_V. It is clear that the hardness is also strongly dependent on E_V. As **Fig. 8**(a) shows, the observed trends in hardness within cuboids

are similar to that of porosity, especially at relatively low E_V values. The Vickers hardnesses of both side and top surfaces are relatively low with relatively large standard deviations when E_V is below 52.08 J/ mm^3, indicating poor melting quality of the Super Invar alloy. As E_V increases to 56.09 J/ mm^3, the Vickers hardnesses of both surfaces remain in the range of 140–160 HV10 with relatively small standard deviations. With further increase in E_V, two pronounced peaks in Vickers hardness at E_V = 63.66 and 89.29 J/mm^3 could be observed. Moreover, the hardnesses of top surfaces are generally lower than those of the side ones at relatively low E_V values ($<$52.08 J/mm^3), and the hardness anisotropy weakens with the increasing E_V, which is in good agreement with the observed anisotropy in porosity.

Fig. 8(b) compares the Vickers hardnesses of as-built cuboids and bars. The elongated bars all show much higher Vickers hardness than their small cuboid counterparts, and large bars show stronger hardness anisotropy than small bars, denoting the influence of LPBF built volumes on microstructural thermal histories of the Super Invar alloy. Especially, the Vickers hardnesses of side surfaces are generally lower than those of top ones in both the vertical-built and horizontal-built bars. It is also highlighted in **Fig. 8**(b) that two notable peaks in the Vickers hardness values appear over the E_V ranges of 61.55–63.66 and 81.85–89.29 J/mm^3 for the cuboids and large-scale bars, respectively. The mechanism for the higher hardness in these two different ranges or the abnormal hardness decline around E_V = 74.40 J/mm^3 within the E_V range of 63.66–81.85 J/mm^3 needs further investigations.

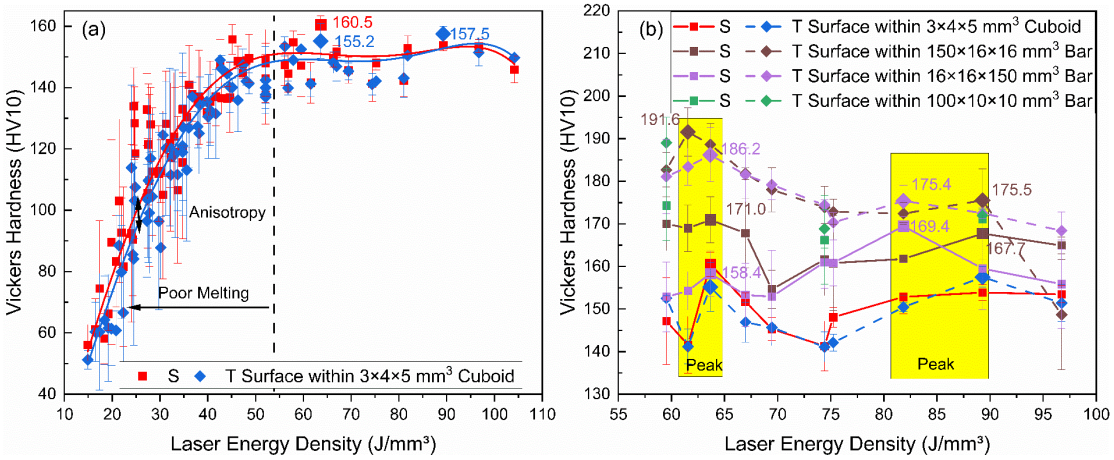


Fig. 8. Variation of Vickers hardness with volumetric laser energy densities within (a) all 72 groups of as-built cuboids (b) as-built cuboids and elongated bars.

3.6 Tensile properties, fractographic analysis, and microstructural characterization

Fig. 9 shows the room-temperature tensile test results and photographs of the tested Super Invar specimens fabricated within the laser energy density range of 59.52–96.73 J/mm^3. As clearly seen from **Fig. 9**(a), the horizontal-built samples machined from the 150×16×16 mm^3 bars are generally found to exhibit superior tensile strengths (both 0.2% YS and UTS), but poorer elongations to failure, as compared with the vertical-built samples machined from the 16×16×150 mm^3 bars. This mechanical anisotropy phenomenon in tensile properties has been widely reported for many other LPBF materials[39, 61, 62]. Nevertheless, even fabricated at the same E_V and tested following the same ASTM standards, small-scale horizontal-built samples (30 mm gauge length and 6 mm gauge diameter, as-built size: 100×10×10 mm^3) evidently show superior elongation but lower tensile strengths as compared with their large bar counterparts (45 mm gauge length and 9 mm gauge diameter, as-built size: 150×16×16 mm^3). This observation, again, confirms the critical role of build size on the mechanical properties of Super Invar alloy fabricated via LPBF. **Fig. 9**(b) records the macroscopic fracture morphology of tensile specimens. All the specimens manufactured from large bar samples within the E_V range of 59.52–96.73 J/mm^3 show a slant fracture feature with necking characteristics, indicating ductile fractures despite different building directions.

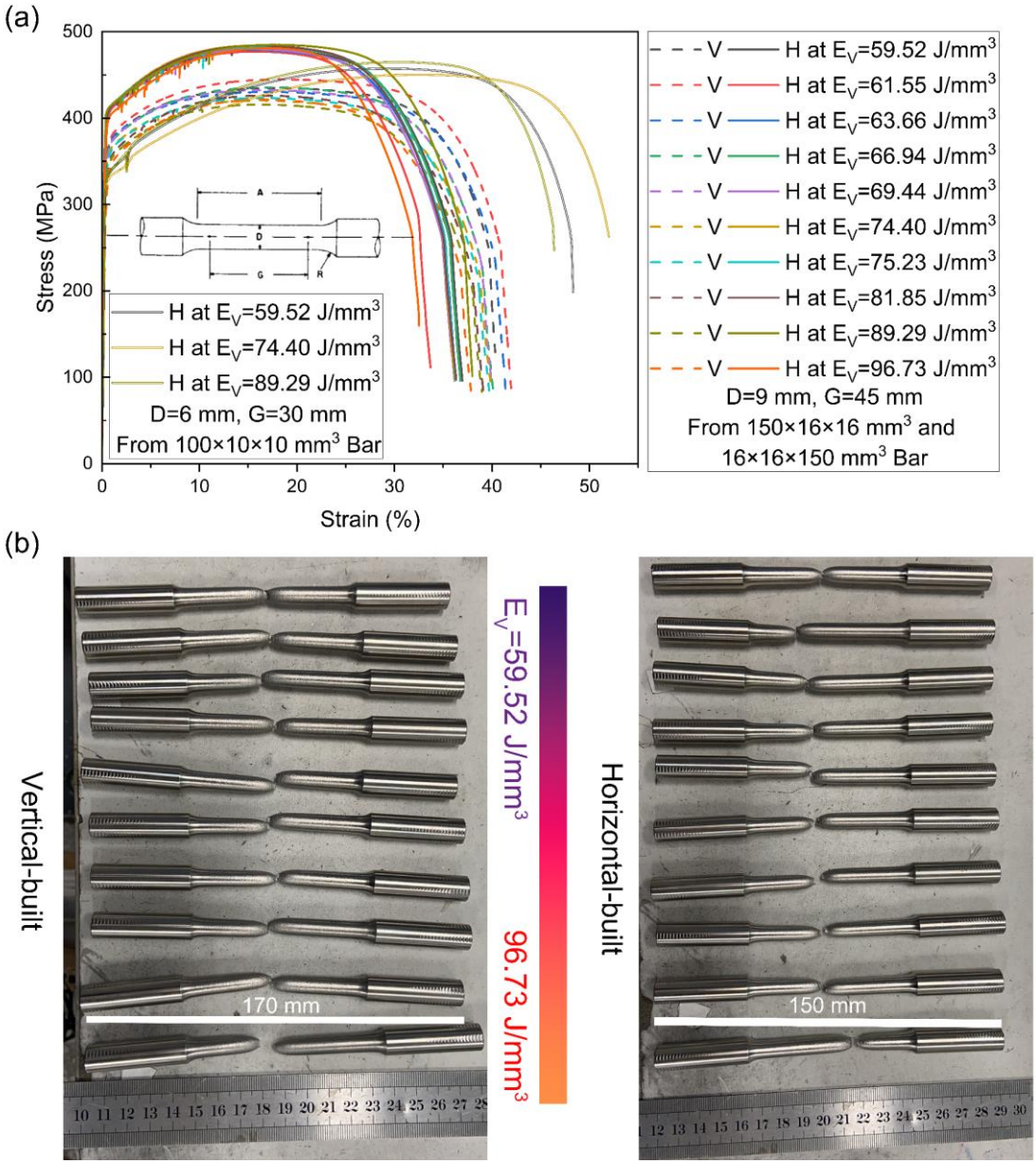


Fig. 9. (a) Tensile stress-strain curves for the vertical-built and horizontal-built different-scale bar samples fabricated at different laser energy densities, (b) macroscopic fracture morphology of large-scale bar samples

Fig. 10 summarizes the *E*, YS, UTS, and elongation to failure data extracted from the recorded stress-strain curves of different Super Invar bar samples. As **Fig. 10**(a) shows, the *E* of horizontal-built samples is generally higher than that of vertical-built ones. It is also noted that the porosity on the side surfaces along the vertical direction is higher than that in top surfaces (see **Fig. 6**(b)), suggesting a strong correlation between the tensile properties and the porosity. For the large-scale bar samples, the

maximum horizontal E (150.6 GPa), together with the lowest porosity within top surfaces occurs at E_V = 63.66 J/mm^3, while the maximum vertical E (138.6 GPa) and the lowest porosity within side surfaces could be identified at E_V = 74.40 J/mm^3, as **Fig. 10**(a) and Fig. **6**(b) show. It is also noted that another small peak in E (106.2 GPa) arises at E_V = 63.66 J/mm^3 for vertical-built large bars, which may be attributed to the lowest porosity in top surface despite relatively poor melting quality observed on the side surface. Peaks in E of both vertical-built and horizontal-built large-scale bar samples are both narrow, revealing the E of Super Invar samples with large building volumes is sensitive to E_V variation. Besides, small-scale horizontal-built bars show much higher E than large-scale ones, which also agrees well with the porosity differences that occur with the build size for Super Invar LPBF process (See Fig. **6**(b)). The E values of small horizontal-built specimens reach 156.2 GPa at E_V = 74.40 J/mm^3 and 148.3 GPa at E_V = 89.29 J/mm^3, which are even higher than that of wrought Super Invar alloy (~144 GPa), indicating the potential application advantage of small-scale Super Invar parts fabricated via LPBF.

As shown in **Fig. 10** (b) and (c), for large-scale specimens, the UTSs are generally positively correlated with the YSs of all Super Invar tensile specimens. Tensile strengths of horizontally built samples remain invariant (UTS ~480 MPa and YS ~395 MPa) within the E_V range of 59.52–96.73 J/mm^3 and reach the maximum (UTS 485.0 MPa and YS 403.7 MPa) at E_V = 89.29 J/mm^3. The tensile strengths of the vertical bars (UTS ~430.0 MPa and YS ~340 MPa) drop (by about ~30 MPa for both UTS and YS) with further increase in E_V after the peak at E_V = 61.55 J/mm^3. It should be emphasized that these two critical E_V points for tensile strengths of vertical and horizontal bars are located within the E_V range of high hardness. The strengths of wrought Super Invar (generally UTS 430.0–480.0 MPa and YS 230–260 MPa)[3, 63, 64] are comparable to the LPBF Super Invar alloy.

As shown in **Fig. 10**(d), the elongations of Super Invar samples at E_V = 96.73 J/mm^3 are poor, indicating over-melting under this condition. The highest elongations

of vertical-built and horizontal-built samples again appear at E_V = 61.55 and 89.29 J/mm^3, respectively, revealing excellent mechanical performance in view of their also remarkable tensile strengths. Generally, all tensile specimens show very good ductility with elongations always higher than 30%[63, 65].

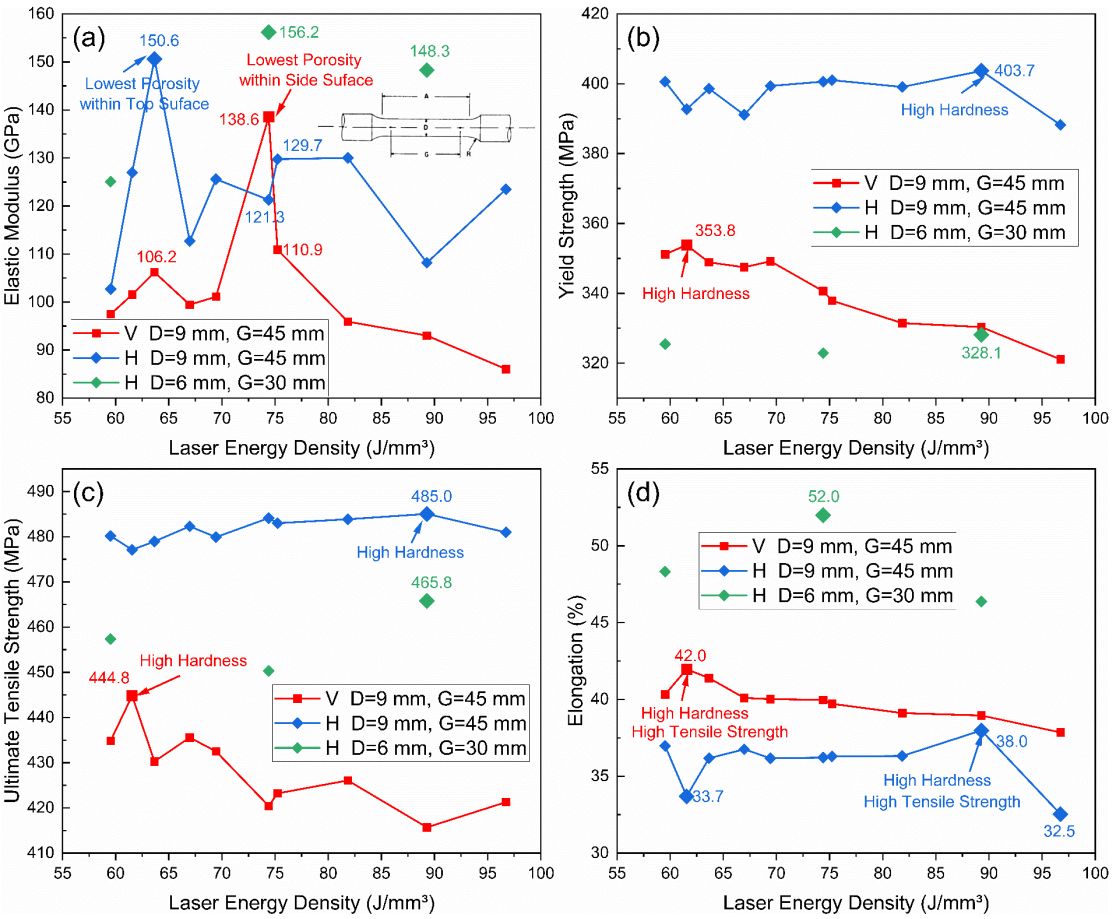


Fig. 10. Influence of the laser energy density on the (a) elastic modulus, (b) yield strength, (c) ultimate strength, and (d) elongation of vertical-built (V) and horizontal-built (H) different-scale bar samples.

Representative fractographies of the tensile specimens are shown in **Fig. 11**. Dimples are observed in all of them, further confirming the ductile nature of the alloy (see **Fig. 9**(b)). As marked in **Fig. 11**, big pores are seldomly found on the fracture surfaces of the vertical-built and horizontal-built specimens with the highest E and lowest porosity.

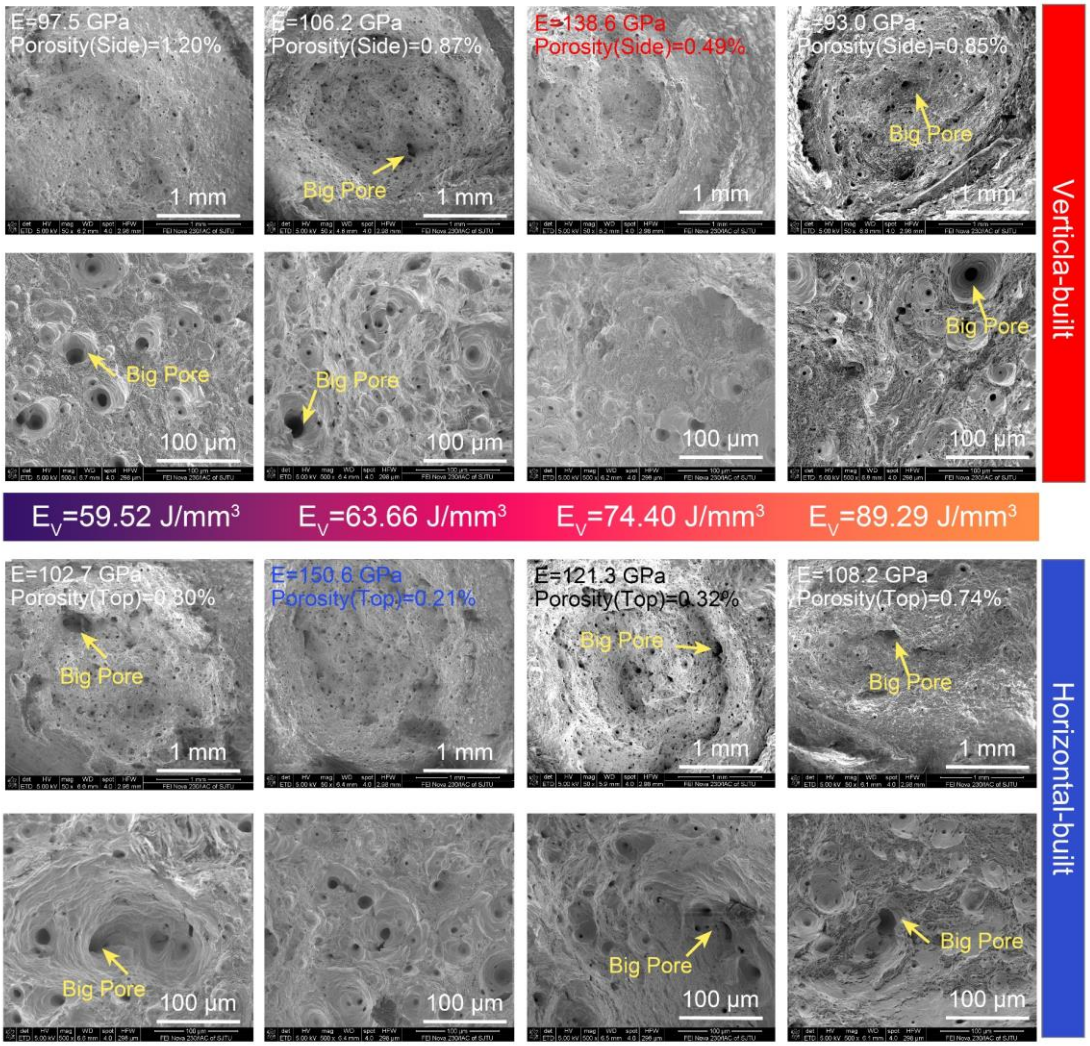


Fig. 11. Fractography of vertical-built and horizontal-built large-scale tensile specimens

Since high stiffness is a critical requirement for Super Invar alloy in semiconductor equipment, the optimum E_V of 74.40 J/mm^3 was then further utilized for fabricating components with relatively high stiffness along both vertical and horizontal directions (horizontal E 121.3 GPa and vertical E 138.6 GPa for the large-scale tensile specimen, horizontal E 156.2 GPa for the small-scale one), combined with relatively low mechanical anisotropy.

Despite the probable location- or build-height-dependence of the microstructural features caused by strong heat accumulation[40, 41, 66] and the critical limitations of using the single E_V as a design parameter for LPBF[67], only the observed surfaces within the

large-scale vertical-built tensile sample (as-built size: 16×16×150 mm^3) fabricated at E_V = 74.40 J/mm^3 were selected for further EBSD investigation for the sake of checking the validity of this set of LPBF parameters. The results are shown in **Fig. 12**. The as-fabricated sample possesses single γ phase (~99% solved for both cross and longitudinal sections) without α precipitates or Co-Fe phase, as shown in **Fig. 12**(a) and (b). This result agrees well with the XRD results (see **Fig. 5**) on the 16×16×150 mm^3 bar sample, and is slightly different from that of the classical Invar 36 (~95% γ phase with 5% α phase)[26]. In **Fig. 12**(c) and (d), the colors red, green, and blue correspond to the grain orientations parallel to [100], [101], and [111] crystallographic axes, respectively. The region with the equiaxed grains in top surface predominantly exhibits <100> and <111> orientations (with the former orientation being more dominant), while the columnar grains observed on the side surface do not display a preferential orientation. **Fig. 12**(e) and (f) compare the grain sizes within the cross and longitudinal sections. The average size of the equiaxed grains on the top surface (42.4 μm) is slightly smaller than that of the columnar grains on the side surface (52.4 μm), which may have contributed to the higher hardness in the top surface (see **Fig. 8**(b)) according to grain boundary strengthening mechanism quantified through the Hall-Petch relation. Compared to the LPBF Invar 36 alloy with an average grain size of 46.4 μm for top surface and 110.5 μm for the side surface[68], our Super Invar alloy obtained at E_V = 74.40 J/mm^3 possesses finer grains. No obvious textures could be observed in the pole figures of both areas, as shown in **Fig. 12**(g) and (h).

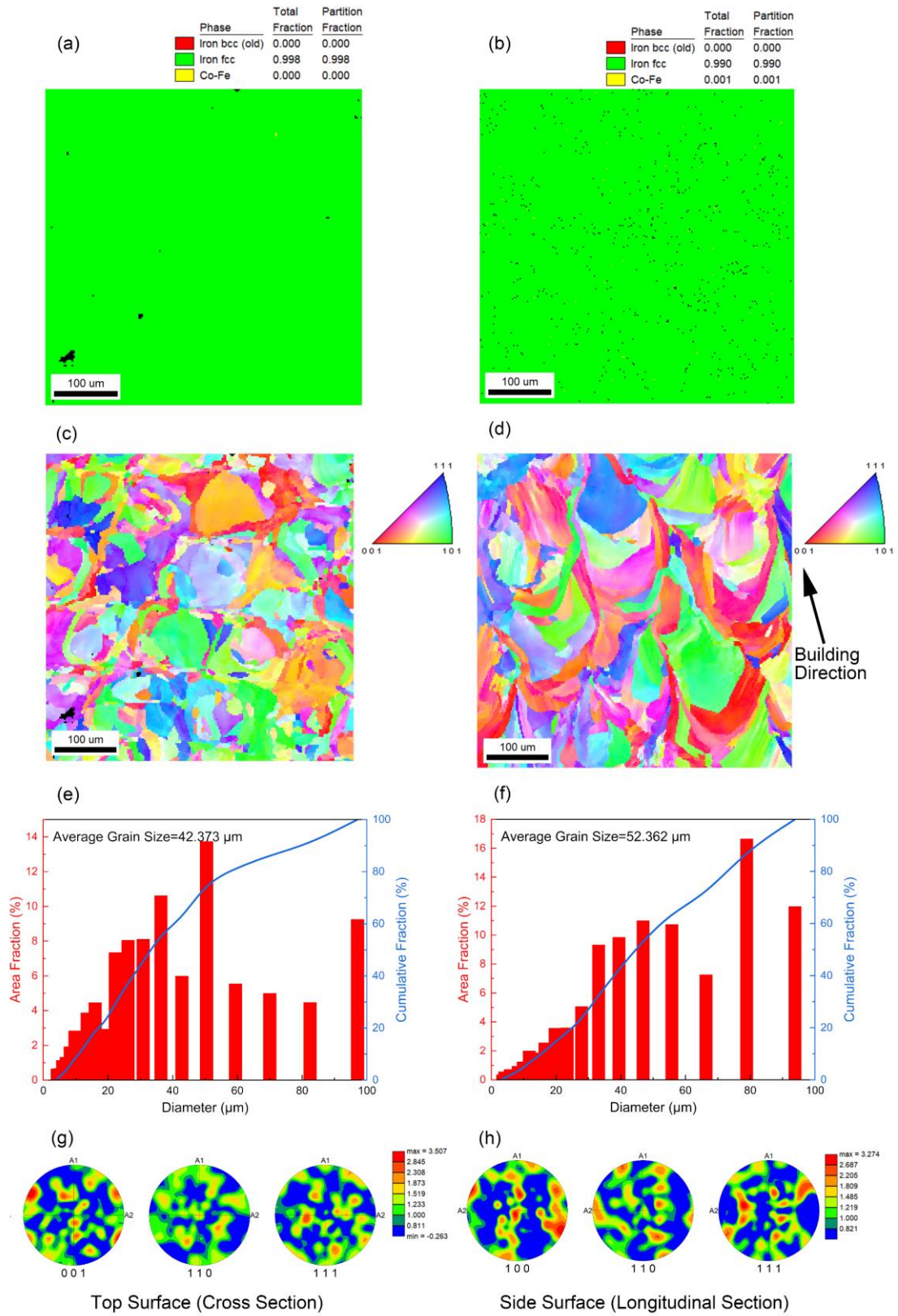


Fig. 12. (a) (b) EBSD phase maps, (c) (d) micrographs, (e) (f) grain size histograms and (g) (h) pole figures of top and side surfaces, respectively, in the

16×16×150 mm^3 bar sample fabricated at E_V = 74.40 J/mm^3.

3.7 Thermal expansion behavior

Thermal expansion measurements were performed on the as-built and standard heat-treated Super Invar samples fabricated at E_V = 74.40 J/mm^3. The measured thermal expansion curves along with the reference lines are shown in **Fig. 13**. Despite the data fluctuation due to the nanometer-level expansion of samples and relatively low detection accuracy of the thermomechanical analyzer, the average CTEs (over the temperature range of 20–100 °C) of the as-built and standard heat-treated samples are approximately −0.17×10^{-6} and 0.52×10^{-6} °C^{-1} respectively. Both are well below 1.0×10^{-6} °C^{-1} required, per Chinese YB/T 5241-2014 Standard[48]. This excellent CTE of the LPBF Super Invar could meet the thermal-induced dimensional-control requirements in the lithography machines and most other high-precision devices. However, the standard heat treatment process slightly increases CTE, which is abnormal compared to wrought or cast Super Invar only showing a lower CTE after the standard heat treatment[69-72]. Further work still needs to be done on this issue combined with the negative thermal expansion behavior of the as-built Super Invar alloy.

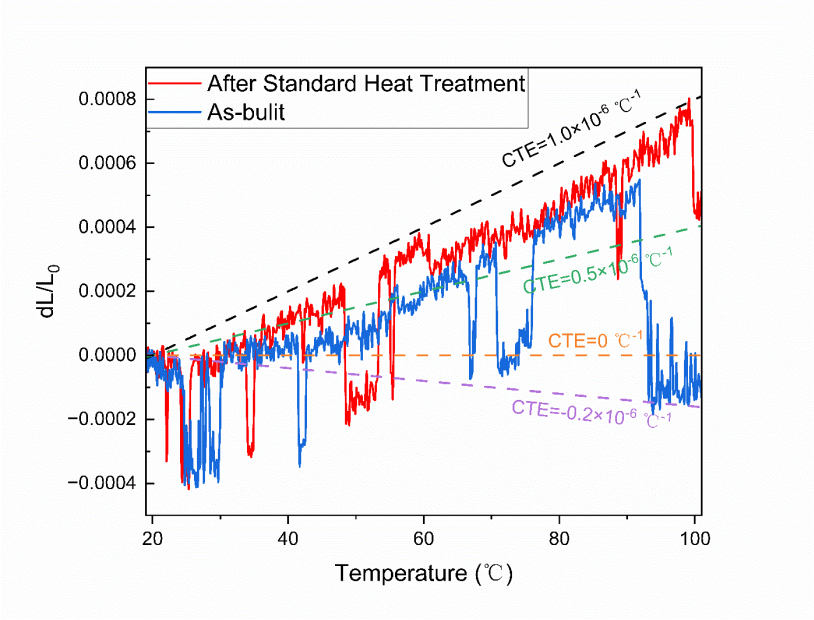


Fig. 13. Thermal expansion results of as-built and standard heat-treated samples

at E_V = 74.40 J/mm^3.

4 Application Verification

4.1 Density evaluation and temporal dimensional stability

As concluded from the tensile and thermal expansion behavior of Super Invar samples, the optimum E_V was identified to be 74.40 J/mm^3, and hence its parametric combination of P = 250 W and v =700 mm/s was then employed for building the mirror-holder used in the lithography machines, as displayed in **Fig. 14**. **Fig. 14**(a) shows the basic dimensions and calculated theoretical volume of the designed part's CAD model. **Fig. 14**(b) shows an image of this as-built Super Invar optical mount. It should be noted that its build height (155 mm) is close to that of the vertical-built tested bars (150 mm). Since the heat treatment procedure suggested in the Chinese YB/T 5241-2014 Standard[48] may increase the thermal expansion of the LPBF-fabricated Super Invar alloy, a simple annealing process at 100 ℃ for 2 h was utilized instead for stress relief of the built part after its wire cutting from the base plate. Next, the Super Invar mirror mount was fine-machined and nickel-plated after sand blasting. An image of the finished product is shown in **Fig. 14**(c). Finally, this high-precision part was integrated into a lithography machine, as **Fig. 14**(d) shows.

On the basis of the measured weight of the final part (710.0 g) and the theoretical volume calculated from its CAD model (88575.8 mm^3), a density of approximately 8.016 g/cm^3 was obtained, which is marginally lower than that of the forged Fe-32Ni-4Co bulk sample (8.10–8.15 g/cm^3). A volumetric porosity of as high as 1.03–1.64% could then be inferred, which coincides with the porosity fraction found in the elongated bars (see **Fig. 6**(b)), proving the non-negligible influence of building geometry on the quality of the LPBF Super Invar alloy.

All the 25 critical dimensional parameters for this integrated part, including size, flatness, verticality, parallelism, and symmetry have been measured four times over a

period of three years. Typical dimensional vibrations, provided in **Fig. 14**(a) for reference, are within the measurement accuracy (0.9 μm) of the Zeiss PRISMO CMM. Thus, this LPBF Super Invar part for optical mounts qualifies as a viable means, despite the simplified heat treatment process conducted in present study.

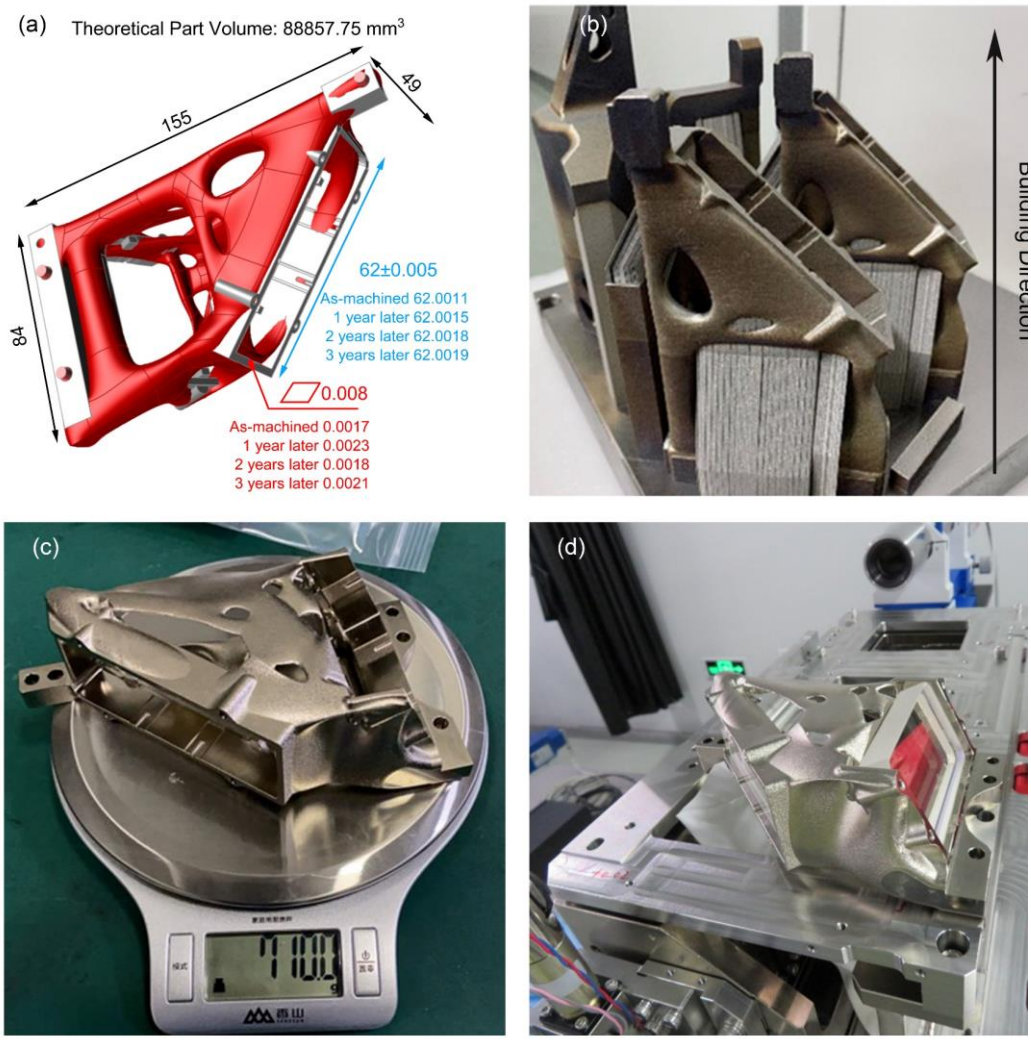


Fig. 14. (a) Model dimension (b) as-built state (c) fine-machined state (d) working condition of the Super Invar mirror-holder fabricated via LPBF

4.2 Modal analysis

Fig. 15 shows the experimental process and the FRF results of the modal tests. The tested Super Invar optical holder was placed on a foam cushion, and the accelerometer was glued on the component along its build direction for recording the

FRF signals during each hammer excitation, as **Fig. 15**(a) displays. The impact hammer test was executed at three different excitation positions to ensure full responses of free vibration at each modal order and identify the free-frequencies of this component in a systematic manner. The free-frequency peaks within the studied range of 1000–5000 Hz were then calibrated from these obtained excitation frequency maps, as marked in **Fig. 15**(b), (c) and (d)[50, 51]. Generally, the nature frequency of the mirror-holder along the Z direction is slightly higher than those along the X and Y directions at the same order, suggesting higher material stiffness along the build direction, which agrees well with the stiffness anisotropy (horizontal E 121.3 GPa and vertical E 138.6 GPa) observed on the specimens fabricated at $E_V = 74.40$ J/mm^3.

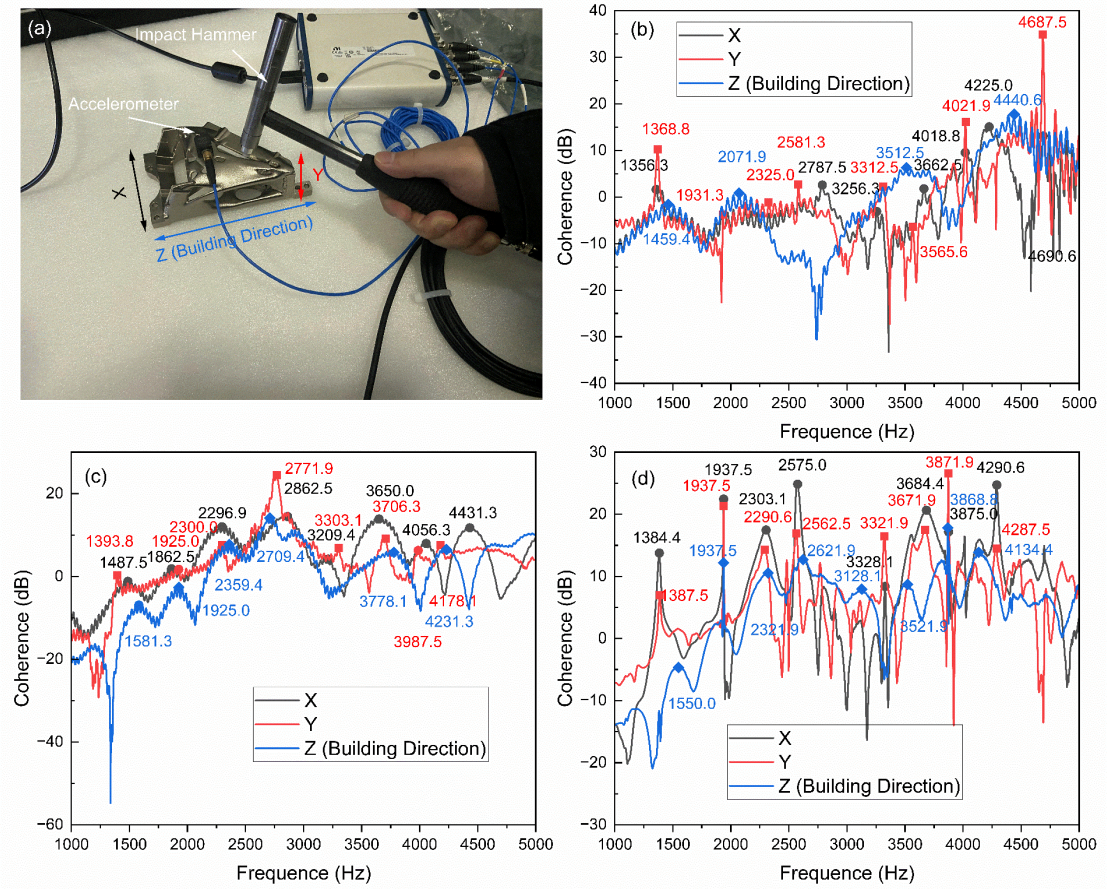


Fig. 15. (a) Impact hammer test on the Super Invar mirror-holder, and (b) (c) (d) frequency maps measured at three different excitation positions.

Fine tetrahedral elements were employed to mesh the CAD model for accurate

dynamic simulation. **Fig. 16** compares the experimental modal test and the corresponding FEA results. As **Fig. 16**(a) and (b) show, the shape of the first-order modal shape obtained from the impact test, which is the most important one, coincides with the FEA calculated one, supporting the validity of both experimental and simulation results. In order to compare the stiffness performance between the LPBF fabricated components and the forged ones, critical physical parameters such as the E and ρ were assumed to be 144 GPa and 8.10 g/cm^3 for the forged bulk, and then 130 GPa and 8.00 g/cm^3, together with 120 GPa and 8.00 g/cm^3 for LPBF processed Super Invar alloy according to the tensile-test and density evaluation results reported earlier in this paper. Besides, the Poisson's ratio (v) is assumed to be 0.23 (the same as that for the wrought Super Invar alloy despite different fabricating methods). **Fig. 16**(c) shows the theoretical free-frequencies calculated with different sets of the assumed physical parameters and the measured results of the mirror-holder at the first 8 modal orders. For such a detailed application situation, the comprehensive stiffness performance or the equivalent effective elastic modulus of this Super Invar component still could not reach the forged level[51, 73], despite the higher frequency measured along the build direction at the first order. Most of the measured data points are located within the FEA result range using the elastic moduli of 130 and 120 GPa respectively, as could be viewed in **Fig. 16**(c), showing an effective elastic modulus of 120–130 GPa of this Super Invar alloy component. This matches well with the tensile test results (elastic moduli of 121.3 and 138.6 GPa, respectively, in horizontal and vertical orientations) on large-scale bars processed with the same laser energy density. Eliminating the rigidity gap within the LPBF processed and forged Super Invar may account on specific heat treatment and other post-processing methods, which will be further explored in our future work.

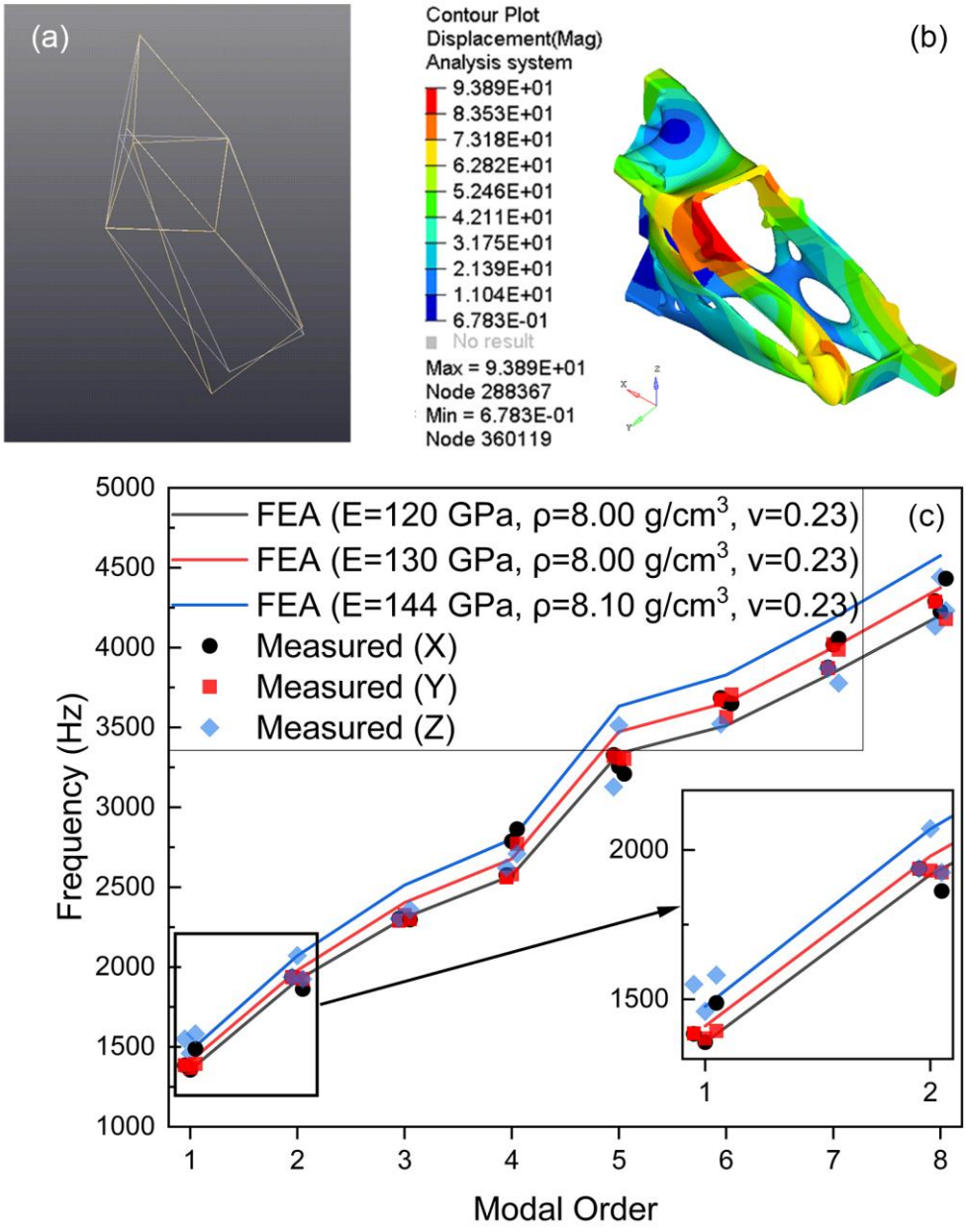


Fig. 16. (a) First-order modal shape obtained from experimental tests, (b) first-order modal shape calculated from FEA results, and (c) comparison of experimentally measured and FEA-calculated free-frequencies at first 8 orders.

5 Conclusions

In the present study, different-scale Super Invar alloy (Fe-32Ni-4Co) samples were fabricated with different combinations of laser power and scanning speed. Several

series of experimental techniques, such as OM, SEM, XRD, ICP, EDS, EBSD, tensile and indentation tests, and thermal expansion measurement were utilized to investigate the influence of process parameters together with building sizes on the microstructures, chemical compositions, constitution phases, porosities, hardnesses, tensile and thermal expansion behaviors of the as-built samples. The carefully selected optimum parameters for comprehensive properties concerned in semiconductor equipment were employed to build a Super Invar mirror-holder for application verification in the lithography machine. The following conclusions can be drawn on the basis of this study:

1. No obvious chemical change or segregation could be observed within LPBF processed Super Invar samples fabricated with the laser energy density of less than 104.17 J/mm^3. The microstructure in the as-fabricated samples was dominated by γ-(Fe-Ni) phase. Very little of abnormal Co-Fe phase could be detected only within the specified-size samples fabricated with specified process parameter.
2. Porosity, hardness and tensile properties of LPBF processed Super Invar alloy are strongly dependent on the volumetric laser energy density despite the parametric combinations of laser power and scanning speed. A positive correlation between the tensile strength and the hardness, together with a negative correlation between the elastic modulus and the porosity within the areas parallel to tensile direction was observed.
3. The increase of building size or volume apparently leads to more porosity, higher hardness, higher tensile strength, lower elongation, and lower horizontal elastic modulus within Super Invar samples fabricated at the same LPBF parameters. This non-negligible influence of building geometry on physical properties of Super Invar alloy samples should be paid sufficient attention in future studies and engineering designs.
4. Due to the poor heat conductivity of Super Invar and the localized nature of the energy distribution of the laser heat source, the critical laser energy for

fully melting the powders between hatch spacings should be higher than that between building layers. With an increased laser energy, acicular or elliptical cracks appeared in side surfaces. This is the reason for the lower porosity observed in the top surfaces compared to that in the side surfaces. It leads to a higher elastic modulus in the horizontal orientation than in vertical orientation. The average grain size of equiaxed grains within top surface is smaller than that of columnar grains within side surface, contributing to superior hardness within top surfaces to that within side ones and better horizontal tensile strengths than vertical ones.

5. The critical E_V for achieving the lowest porosity within side surfaces and the highest vertical elastic modulus is clearly identified to be 74.40 J/mm^3 despite the build height. The critical laser energy density for the lowest porosity within top surfaces decreases with the building area increasing and is located at 63.66 J/mm^3 for the horizontal-built 150×16×16 mm^3 specimen showing the highest horizontal elastic modulus.
6. Fine grains (equiaxed grain size of the top surface: 42.4 μm, columnar grain size of the side surface: 52.4 μm) could be obtained within microstructure of the Super Invar sample fabricated at E_V = 74.40 J/mm^3. The samples manufactured at E_V = 74.40 J/mm^3 also show very low coefficients of thermal expansion within 20–100 °C (-0.17×10^{-6} °C^{-1} for as-built state and 0.52×10^{-6} °C^{-1} for stand heat-treated state, respectively), which fully satisfy the requirements for thermal-induced dimensional control in most of semiconductor equipment.
7. The optimum laser energy density for use in semiconductor equipment is strongly recommended to be 74.40 J/mm^3 (Critical LPBF parameters: laser power 250 W, scanning speed 700 mm/s, layer thickness 0.04 mm, hatch spacing 0.12 mm) due to the comprehensively excellent horizontal and vertical stiffness performance, and relatively high tensile strength in combination with

a low CTE within 20–100℃ of as-fabricated specimens. At this optimum laser energy density, an effective elastic modulus of 120–130 GPa of the 155 mm-in-height Super Invar mirror-holder could be extrapolated based on experimental modal tests and numerical simulation analysis. Specific heat treatment and other post-processing methods should be further studied for eliminating the elastic modulus gap between large-scale LPBF processed (horizontal: 121.3 GPa, vertical:138.6 GPa) and forge (~144 GPa) Super Invar components, considering better applications in semiconductor equipment.

Declaration of Competing Interest

The authors declare that they do not have any commercial or associative interest that could have appeared to influence the work reported in this paper.

Acknowledgement

This work was financially supported by National Key R&D Program of China (No. 2022YFB4602102), Agency for Science, Technology and Research (A*STAR) of Singapore via Structural Metal Alloys Programme (No. A18B1b0061) and Advanced Models for Additive Manufacturing (No. M22L2b0111). We would like to acknowledge the supports from Instrumental Analysis Center of Shanghai Jiao Tong University and Instrument and equipment sharing platform of School of Materials Science and Engineering, SJTU.

References

[1] B. Rui, N. Sakaguchi, N. Nakada, Mechanism of austenite recrystallization induced by martensitic reversion in super invar cast alloy, Materialia 15 (2021).
[2] M. Ferry, Alloys: Iron, Encyclopedia of Condensed Matter Physics2024, pp. 522-532.
[3] C. Li, J. Zheng, S. He, B. Cai, Y. Song, Microstructure and Tensile Properties of the Fe-32%Ni-4%Co Alloy During Cryorolling and Subsequent Annealing, Journal of Materials Engineering and Performance 27(12) (2018) 6657-6664.
[4] Z.Y. Rao, H. Springer, D. Ponge, Z.M. Li, Combinatorial development of multicomponent Invar alloys via rapid alloy prototyping, Materialia 21 (2022).
[5] N. Sakaguchi, H. Ohno, N. Nakada, Strengthening of Super Invar Cast Steel by Precipitation of Intermetallic Compounds, Isij International 62(7) (2022) 1532-1539.
[6] M. Pumphrey, M.A. Saaideh, Y.M. Al-Rawashdeh, N. Alatawneh, M.A. Janaideh, Force modeling of a reluctance motion system with multi-axial asymmetrical air gaps, Precision engineering 86 (2024) 276-284.
[7] Z.Z. Deng, Q. Li, Y. Onuki, Q.P. Sun, Multifunctional nanostructured NiTi alloy with Invar, Elinvar and Rinvar properties, Journal of Alloys and Compounds 909 (2022).
[8] S. Gharazi, B.C. Zarket, K.C. DeMella, S.R. Raghavan, Nature-Inspired Hydrogels with Soft and Stiff Zones that Exhibit a 100-Fold Difference in Elastic Modulus, ACS Appl. Mater. Interfaces 10(40) (2018) 34664-34673.
[9] R.M. Abhilash, G.S. Venkatesh, S.S. Chauhan, Micromechanical modeling of bamboo short fiber reinforced polypropylene composites, Multiscale and Multidiscip. Model. Exp. and Des 4(1) (2021) 25-40.
[10] M. Strangwood, Alloys: Steel, Encyclopedia of Condensed Matter Physics2024, pp. 533-548.
[11] K. Xu, B.C. Li, S.M. Li, R.H. Chen, X.K. Gao, C.H. Liu, C. Jiang, L.J. Song, Excellent tension properties of stainless steel with a 316L/17-4PH/17-4PH laminated structure fabricated through laser additive manufacturing, Materials Science and Engineering a-Structural Materials Properties Microstructure and Processing 833 (2022).
[12] A. Sood, J. Schimmel, V.M. Ferreira, M. Bosman, C. Goulas, V. Popovich, M.J.M. Hermans, Directed energy deposition of Invar 36 alloy using cold wire pulsed gas tungsten arc welding: Effect of heat input on the microstructure and functional behaviour, Journal of Materials Research and Technology-Jmr&T 25 (2023) 6183-6197.
[13] G.H. Jiao, X.W. Fang, X.M. Chen, N.Y. Xi, M.G. Zhang, Y. Liu, H.Y. Wu, K. Huang, The origin of low thermal expansion coefficient and enhanced tensile properties of Invar alloy fabricated by directed energy deposition, Journal of Materials Processing Technology 317 (2023).
[14] A. Gil Del Val, X. Cearsolo, A. Suarez, F. Veiga, I. Altuna, M. Ortiz, Machinability characterization in end milling of Invar 36 fabricated by wire arc additive manufacturing, Journal of Materials Research and Technology 23 (2023) 300-315.

[15] J. Zhu, H. Kokawa, K. Feng, Z. Li, Unexpectedly high corrosion susceptibility near fusion boundaries of Inconel 625 manufactured by laser powder bed fusion, Corrosion Science 223 (2023).
[16] C.C. Zhang, K. Feng, H. Kokawa, B. Han, Z.G. Li, Cracking mechanism and mechanical properties of selective laser melted CoCrFeMnNi high entropy alloy using different scanning strategies, Materials Science and Engineering a-Structural Materials Properties Microstructure and Processing 789 (2020).
[17] G. Liu, X. Zhang, X. Chen, Y. He, L. Cheng, M. Huo, J. Yin, F. Hao, S. Chen, P. Wang, S. Yi, L. Wan, Z. Mao, Z. Chen, X. Wang, Z. Cao, J. Lu, Additive manufacturing of structural materials, Materials Science and Engineering: R: Reports 145 (2021).
[18] Z. Snow, A.R. Nassar, E.W. Reutzel, Invited Review Article: Review of the formation and impact of flaws in powder bed fusion additive manufacturing, Additive Manufacturing 36 (2020).
[19] M.J. Paul, J.J. Kruzic, U. Ramamurty, B. Gludovatz, The importance of fracture toughness evaluation for additively manufactured metals, Acta Materialia 276 (2024).
[20] D.-H. Lee, J.Y. Jung, K.H. Lee, S.Y. Lee, Y. Zhao, K.B. Lau, P. Wang, U. Ramamurty, Distinct effects of in-situ and ex-situ hydrogen charging methods on the mechanical behavior of CoCrFeNi high-entropy alloy fabricated by laser-powder bed fusion, Journal of Alloys and Compounds 940 (2023).
[21] M. Watson, M. Leary, D. Downing, M. Brandt, Generative design of space frames for additive manufacturing technology, International Journal of Advanced Manufacturing Technology 127(9-10) (2023) 4619-4639.
[22] B. Dutta, S. Babu, B. Jared, Design for metal additive manufacturing, Science, Technology and Applications of Metals in Additive Manufacturing2019, pp. 193-244.
[23] E.M. Parsons, Lightweight cellular metal composites with zero and tunable thermal expansion enabled by ultrasonic additive manufacturing: Modeling, manufacturing, and testing, Composite Structures 223 (2019).
[24] S. Wei, C. Hutchinson, U. Ramamurty, Mesostructure engineering in additive manufacturing of alloys, Scripta Materialia 230 (2023).
[25] Y. Zhao, K.B. Lau, W.H. Teh, J.J. Lee, F. Wei, M. Lin, P. Wang, C.C. Tan, U. Ramamurty, Compositionally graded CoCrFeNiTi high-entropy alloys manufactured by laser powder bed fusion: A combinatorial assessment, Journal of Alloys and Compounds 883 (2021).
[26] C.L. Qiu, N.J.E. Adkins, M.M. Attallah, Selective laser melting of Invar 36: Microstructure and properties, Acta Materialia 103 (2016) 382-395.
[27] C.L. Qiu, Y.J. Liu, H.H. Liu, Influence of addition of TiAl particles on microstructural and mechanical property development in Invar 36 processed by laser powder bed fusion, Additive Manufacturing 48 (2021).
[28] M. Yakout, A. Cadamuro, M.A. Elbestawi, S.C. Veldhuis, The selection of process parameters in additive manufacturing for aerospace alloys, International Journal of Advanced Manufacturing Technology 92(5-8) (2017) 2081-2098.
[29] M. Yakout, M.A. Elbestawi, S.C. Veldhuis, A study of thermal expansion

coefficients and microstructure during selective laser melting of Invar 36 and stainless steel 316L, Additive Manufacturing 24 (2018) 405-418.
[30] M. Yakout, M.A. Elbestawi, S.C. Veldhuis, Density and mechanical properties in selective laser melting of Invar 36 and stainless steel 316L, Journal of Materials Processing Technology 266 (2019) 397-420.
[31] M. Yakout, I. Phillips, M.A. Elbestawi, Q.Y. Fang, In-situ monitoring and detection of spatter agglomeration and delamination during laser-based powder bed fusion of Invar 36, Optics and Laser Technology 136 (2021).
[32] N.J. Harrison, I. Todd, K. Mumtaz, Thermal expansion coefficients in Invar processed by selective laser melting, Journal of Materials Science 52(17) (2017) 10517-10525.
[33] H. Asgari, M. Salarian, H. Ma, A. Olubamiji, M. Vlasea, On thermal expansion behavior of invar alloy fabricated by modulated laser powder bed fusion, Materials & Design 160 (2018) 895-905.
[34] Q.D. Yang, K. Wei, X.J. Yang, H.Q. Xie, Z.L. Qu, D.N. Fang, Microstructures and unique low thermal expansion of Invar 36 alloy fabricated by selective laser melting, Materials Characterization 166 (2020).
[35] K. Wei, Q.D. Yang, B. Ling, X.J. Yang, H.G. Xie, Z.L. Qu, D.N. Fang, Mechanical properties of Invar 36 alloy additively manufactured by selective laser melting, Materials Science and Engineering a-Structural Materials Properties Microstructure and Processing 772 (2020).
[36] T. Wegener, F. Brenne, A. Fischer, T. Moller, C. Hauck, S. Auernhammer, T. Niendorf, On the structural integrity of Fe-36Ni Invar alloy processed by selective laser melting, Additive Manufacturing 37 (2021).
[37] L. Hitzler, M.Z.S. Hameed, A. Kah, M. Merkel, E. Werner, Thermal expansion and temperature-dependent Young's modulus of Invar fabricated via laser powder-bed fusion, Progress in Additive Manufacturing 7(3) (2022) 463-470.
[38] Q. Yang, S. Yang, S. Ma, J. Zhou, Y. Zhou, R. Huang, K. Wei, Z. Qu, X. Yang, In-situ X-ray computed tomography tensile tests and analysis of damage mechanism and mechanical properties in laser powder bed fused Invar 36 alloy, Journal of Materials Science & Technology 175 (2024) 29-46.
[39] G. Huang, G. He, Y. Liu, K. Huang, Anisotropy of microstructure, mechanical properties and thermal expansion in Invar 36 alloy fabricated via laser powder bed fusion, Additive Manufacturing 82 (2024).
[40] M. Kusano, Y. Takata, A. Yumoto, M. Watanabe, Effects of time per layer and part geometry on thermal history and microcracking in the fabrication of nickel superalloy samples by laser powder bed fusion, Additive Manufacturing 80 (2024).
[41] D. Bartels, T. Novotny, M. Albert, A. Mohr, F. van Soest, H. Hill, C. Merklein, M. Schmidt, Effect of Volumetric Energy Density and Part Height on the Material Properties of Low-Alloyed Steels Manufactured by Laser-Based Powder Bed Fusion of Metals, Advanced Engineering Materials 25(21) (2023).
[42] Y. Xu, D. Zhang, J. Deng, X. Wu, L. Li, Y. Xie, R. Poprawe, J.H. Schleifenbaum,

S. Ziegler, Numerical Simulation in the Melt Pool Evolution of Laser Powder Bed Fusion Process for Ti6Al4V, Materials 15(21) (2022).
[43] M.A. Chaudry, G. Mohr, K. Hilgenberg, Experimental and numerical comparison of heat accumulation during laser powder bed fusion of 316L stainless steel, Progress in Additive Manufacturing 7(5) (2022) 1071-1083.
[44] M.F. Ashby, Materials Selection in Mechanical Design (4th Edition), 4th ed., San Diego: Elsevier, San Diego, 2010.
[45] E384 Standard Test Method for Microindentation Hardness of Materials, 2017.
[46] F3122 Standard Guide for Evaluating Mechanical Properties of Metal Materials Made via Additive Manufacturing Processes, 2014.
[47] E8/E8M Standard Test Methods for Tension Testing of Metallic Materials, 2016.
[48] Iron-nickel and iron-nickel-cobalt alloys with low expansion (Written in Chinese), Central Iron & Steel Research Institute; China Metallurgical Information and Standardization Institute, 2014.
[49] U. Diala, Y. Zhu, R. Gunawardena, Investigative Study of the Effect of Damping and Stiffness Nonlinearities on an Electromagnetic Energy Harvester at Low-Frequency Excitations, Machines 12(1) (2024).
[50] E.-T. Lee, Y.-S. Hong, H.-C. Eun, Prediction of the Physical Properties of a Structural Member by the Impact Hammer Test, Sensors 22(18) (2022).
[51] M. Merhar, Determination of Elastic Properties of Beech Plywood by Analytical, Experimental and Numerical Methods, Forests 11(11) (2020).
[52] S.F. Jacobs, S.C. Johnston, D.E. Schwab, Dimensional instability of Invars, Appl Opt 23(20) (1984) 3500.
[53] J.M. Steele, D.A. Thompson, S.F. Jacobs, D.L. Bass, Temperature and age effects on the temporal stability of Invar, SPIE, pp. 40-51.
[54] Q. Wang, Y.W. Dong, Z.H. Jiang, J. Huang, Enhancing low thermal expansion behavior and strength via induced Zr-rich intermetallic phase in Fe-36Ni Invar alloy, Materials & Design 226 (2023).
[55] Precision alloys—Designation (Written in Chinese), State Administration for Market Regulation；Standardization Administration of the People's Republic of China, 2019.
[56] T. Liu, Z.A.N. Gao, W.L. Ling, Y.N. Wang, X.M. Wang, X.H. Zhan, Effect of heat accumulation on the microstructure of Invar alloy manufactured by multi-layer multi-pass laser melting deposition, Optics and Laser Technology 144 (2021).
[57] Z.Y. Rao, D. Ponge, F. Kormann, Y. Ikeda, O. Schneeweiss, M. Friak, J. Neugebauer, D. Raabe, Z.M. Li, Invar effects in FeNiCo medium entropy alloys: From an Invar treasure map to alloy design, Intermetallics 111 (2019).
[58] X.X. Rao, Y.D. Ru, F.M. Guo, Y. Ren, L.S. Cui, K.Y. Yu, Abnormal strain evolution of austenite upon martensitic transformation in FeNiCo alloy with invar effect: An in situ study, Scripta Materialia 220 (2022).
[59] D. Sun, J. Li, X. Hao, M. Wang, D. Li, X. Sun, Z. Yang, T. Wang, F. Zhang, Effect of Cold Rolling and Cryogenic Treatment on the Microstructure and Mechanical

Properties of Fe–32Ni Alloy, Metals 14(2) (2024).
[60] C. Hagenlocher, P. O'Toole, W. Xu, M. Brandt, M. Easton, A. Molotnikov, Analytical modelling of heat accumulation in laser based additive manufacturing processes of metals, Additive Manufacturing 60 (2022).
[61] M.R. Condruz, G. Matache, A. Paraschiv, T.F. Frigioescu, T. Badea, Microstructural and Tensile Properties Anisotropy of Selective Laser Melting Manufactured IN 625, Materials 13(21) (2020).
[62] K.-S. Kim, J.-W. Hwang, K.-A. Lee, Effect of building direction on the mechanical anisotropy of biocompatible Co–Cr–Mo alloy manufactured by selective laser melting process, Journal of Alloys and Compounds 834 (2020).
[63] R.K. Gupta, P. Varma, V. Anil Kumar, P. Sarkar, J. Desai, P. Ramkumar, Processing and Characterization of Superinvar for Space Application, Materials Science Forum 830-831 (2015) 30-33.
[64] N. Sakaguchi, H. Ohno, N. Nakada, Simultaneous Optimization of Rigidity and Strength of Super Invar Cast Steel using by Martensitic Reversion, ISIJ International 62(3) (2022) 586-592.
[65] M. Kutz, Mechanical Engineers' Handbook, Volume 1 - Materials and Engineering Mechanics (4th Edition), 4 ed., Newark: John Wiley & Sons, Newark, 2015.
[66] R. Ranjan, C. Ayas, M. Langelaar, F. van Keulen, Fast Detection of Heat Accumulation in Powder Bed Fusion Using Computationally Efficient Thermal Models, Materials 13(20) (2020).
[67] U. Scipioni Bertoli, A.J. Wolfer, M.J. Matthews, J.-P.R. Delplanque, J.M. Schoenung, On the limitations of Volumetric Energy Density as a design parameter for Selective Laser Melting, Materials & Design 113 (2017) 331-340.
[68] M. Kul, B. Akgul, Y.Z. Karabay, The relationship of hot and cold rolling processes with the structure and properties of invar 36, Materials Chemistry and Physics 295 (2023).
[69] B. Akgul, M. Kul, F. Erden, The puzzling thermal expansion behavior of invar alloys: a review on process-structure-property relationship, Critical Reviews in Solid State and Materials Sciences ahead-of-print(ahead-of-print) (2023) 1-54.
[70] G. Huang, G. He, X. Gong, Y. He, Y. Liu, K. Huang, Additive manufacturing of Invar 36 alloy, Journal of materials research and technology 30 (2024) 1241-1268.
[71] I. Rishmawi, A. Rogalsky, M. Vlasea, M. Salarian, S. Bakhshivash, The Effects of Heat Treatment on Tensile and Thermal Expansion Behavior of Laser Powder-Bed Fusion Invar36, Journal of Materials Engineering and Performance 31(12) (2022) 9727-9739.
[72] S.H. Lohaus, M. Heine, P. Guzman, C.M. Bernal-Choban, C.N. Saunders, G. Shen, O. Hellman, D. Broido, B. Fultz, A thermodynamic explanation of the Invar effect, Nature Physics 19(11) (2023) 1642-1648.
[73] L. Yuan, S. Liang, Free vibration analysis of embedded and co-cured perforated damping sandwich composite beam, Journal of Composite Materials 55(19) (2021) 2605-2615.